Atomic dynamics in Al-rich Al-Co alloys near the composition of the decagonal quasicrystal

M. Mihalkovič, H. Elhor, and J.-B. Suck
Materials Research and Liquids, Institute of Physics, TU Chemnitz, D-09107 Chemnitz, Germany
(Received 17 October 2000; published 14 May 2001)

We used realistic Al-Co pair potentials [R. Phillips, J. Zou, A. E. Carlsson, and M. Widom, Phys. Rev. B **49**, 9322 (1994); J. A. Moriarity and M. Widom, *ibid.* **56**, 7905 (1997)] to study the atomic dynamics of $Al_{1-x}TM_x$ crystalline structures with the fractional content x of the transition metal (TM) atom $x \lesssim 0.3$. Our list comprises rather simple structures of Al_3Ni and Al_5Co_2 alloys, complex structures related to the decagonal quasicrystal (Al_9Co_2Ni, O-$Al_{13}Co_4$), and a model of the crystalline approximant of the decagonal quasicrystal *d*-AlNiCo. Within the harmonic approximation, we assess the impact of the structural complexity on the phonon density of states, sound velocity, Debye-Waller factor, and the character of the phonon states at low energies. In complex structures related to the decagonal quasicrystal, a significant fraction of low-energy vibrations have nonacoustic, strongly localized character. In a molecular-dynamics annealing of the decagonal approximant model performed at elevated temperature, a fraction of aluminum atoms display signs of diffusive motion, while the equilibrium positions of the cobalt atoms do not change.

DOI: 10.1103/PhysRevB.63.214301 PACS number(s): 61.44.Br, 63.20.−e

I. INTRODUCTION

One representative class of quasicrystals with both decagonal and icosahedral phases are Al-rich aluminides, in which icosahedral *i*-AlPdMn and decagonal *d*-AlNiCo form at certain composition quasicrystalline structures, competing in the perfection of the topological order with good-quality periodic crystals. Understanding the energetic origins of quasicrystal ordering requires comparison of the structural energies of quasicrystal models with energies of the crystalline structures with similar composition. A promising systematic approach is based on recent developments in modeling pair interactions in Al-rich aluminides: semiempirical pair potentials have been designed and tested for Al-Mn (Ref. 3) and Al-Co systems,[1] and *ab initio* generalized pseudopotential theory (GPT) potentials for a range of Al-TM (transition metal) systems.[2] The latter potentials were applied in a study of Al-Ni and Al-Co binary phase diagrams.[4]

In this paper, we report on a complementary exploration, focusing on various aspects of the atomic dynamics in the $Al_{1-x}Co_x$ system, with x ranging up to 0.3. Our primary motivation is to obtain a comprehensive picture of the dependence of the dynamical properties on the structure. The stable phases occurring in the binary Al-Co and Al-Ni and ternary Al-Ni-Co systems with the transition-metal content ranging from $x=0.2–0.3$ provide particularly suitable grounds for such a study: the rather simple crystalline structures of Al_3Ni and Al_5Co_2 stand in contrast to Al_9Co_2Ni and O-$Al_{13}Co_4$ structures with a close relationship to the decagonal quasicrystals near $Al_{70}(Ni,Co)_{30}$ composition.

Although the details of the quasicrystalline structures remain uncertain, the amount of experimental and theoretical work on their vibrational properties (for a review, see Ref. 5) exceeds by far the available information on the crystalline phases at similar compositions, the structures of which are known accurately. In the long-wavelength limit, both icosahedral (*i*-AlPdMn) (Ref. 6) and decagonal (*d*-AlNiCo) (Ref. 7) quasicrystals exhibit ordinary acoustic phonons. In *i*-AlPdMn, the experiment found broad ($\sim$4 meV) optic branches; the one with the lowest energy was at $\sim$8 meV. A spring-model study applied to icosahedral tilings[8] predicted the existence of optic branches with hierarchical structure, with the lowest energy of an optic mode scaling inversely with the size of the approximant unit cell; however, these states had no impact on the phonon density of states that scaled with ω^2 as expected from the Debye approximation, and the low-energy modes had extended character. A study using realistic pair potentials and atomic structure models of Frank–Kasper icosahedral quasicrystals *i*-AlCuLi (Ref. 9) and *i*-AlZnMg (Ref. 10) revealed that besides the propagating excitations there exist other, spatially confined modes, contributing appreciably to the density of states even in the low-energy region. Recently, new experimental evidence of nonacoustic low-energy modes became available: the low-temperature heat capacity of *i*-AlPdMn (Ref. 11) is larger than the Debye value calculated from the sound velocities, and low-energy tunneling states were found from low-temperature variations of the sound velocity in *i*-AlPdMn,[12] *i*-AlCuFe,[13] and *i*-ZnMgY (Ref. 14) quasicrystals. A similar conclusion has been drawn from the comparison of the experimentally determined phonon density of states and model calculations based on a simple structure model of *d*-AlNiCo using the semi-empirical Al-Co pair potentials.[15]

Our paper is organized as follows. In Sec. II, we discuss the choice of the crystalline phases studied in this paper, characterize their structures, and describe a pseudobinary model of quasicrystal approximant in the *d*-Al(NiCo) system. In Sec. II C we introduce semi-empirical[1] and GPT[2] pair potentials. While our selection of the crystalline phases contrasts different structures, a parallel use of the two sets of pair potentials tests the robustness of the conclusions we draw. Section III provides the theoretical background for the standard method we used to assess the dynamical properties: the harmonic analysis via the direct diagonalization of the complex dynamical matrices. Finally, our results are reviewed and discussed in Secs. IV and V.

II. ATOMIC STRUCTURES AND PAIR POTENTIALS

A. Model of quasicrystal approximant

One distinct feature of the decagonal quasicrystal structures near the $Al_{70}(CoNi)_{30}$ composition are the decagonal

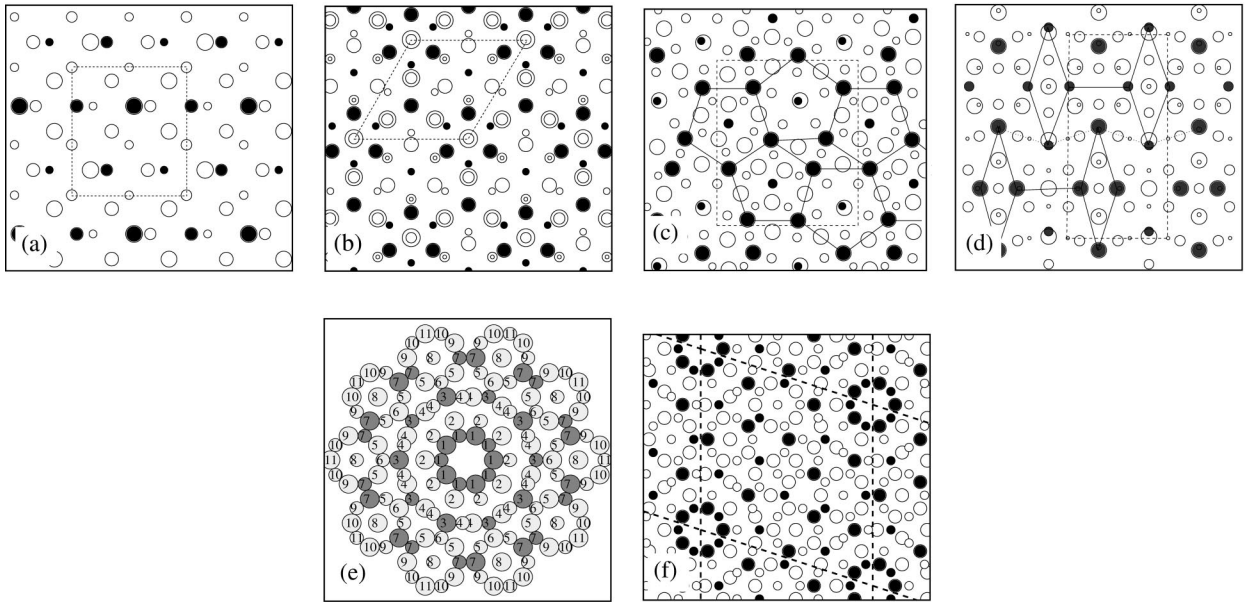

FIG. 1. (a) Structure of Al_3Ni (projection along z axis), (b) Al_5Co_2 (projection along threefold axis), (c) O-$Al_{13}Co_4$ (pseudodecagonal axis), (d) Al_9Co_2Ni (pseudodecagonal axis), (e) the decagonal cluster in the model of the *d*-ANC approximant, and (f) the approximant model of *d*-ANC (pseudodecagonal axis). Dark circles are TM atoms, open circles Al. The radii of the circles scale with the atomic coordinate perpendicular to the plane.

ring contrasts with ~ 20 Å diameter observed in high-resolution transverse-electromagnetic mode (HRTEM) images. The corresponding average structure—a decagonal columnar cluster shown in Fig. 1(e)—has been first resolved in an earlier diffraction refinement study.[16] In the figure, the numbers label symmetry-inequivalent sites. Light-gray circles are Al and filled circles TM atoms. The size of the circles scales with the z coordinate perpendicular to the plane: there are two layers of atoms related by a 10–fold screw symmetry operation. The columnar cluster is built by a translational symmetry operation along the ''periodic'' z axis, with the $c=4.08$ Å period.

We adopt a structural model of the quasicrystal approximant, in which the columnar clusters decorate vertices of the tiling of golden rhombi with acute angles of $\gamma=72°$ and an edge length of $a=19.8$ Å, in a manner similar to the model proposed in Ref. 17 on the basis of the HRTEM images. The choice of this geometrical arrangement of the columnar clusters was motivated by the requirement of simplicity; refinement of the details of quasicrystal structures is beyond the scope of this paper.

The atomic positions generated by the above decoration rule *cover* all the sites actually occupied by the atoms. There are few short-distance conflicts between the atoms in the outer shell of the cluster; one simple and symmetrical way of resolving these conflicts is shown in Fig. 1(f).

We checked the plausibility of the model by comparing the structure factors with the set of 253 diffraction amplitudes reported in Ref. 16. In order to register the quasicrystal and approximant peak positions, we sheared appropriately the four reciprocal basis vectors lying in the quasiperiodic plane. The weighted R factor resulting from a nonlinear least-squares fit was $R_w=0.151$ using only three parameters: Debye-Waller factors $B_{Al}=2.78$, $B_{TM}=0.61$ Å^2, and an overall scale factor. The aptness of the fit is illustrated in Fig. 2, showing a semilogarithmic plot of the calculated vs measured structure factors. When we increased the number of parameters and refined an independent Debye-Waller factor for each of the 11 orbits, the fit improved only by $\sim 1\%$. Interestingly, using a subset of only 47 measured reflections in the 0th Laue zone, R_w increased by more than 5%.

The atomic density of the model (see Table I) is very close to that of $Al_5Co_2$and appreciably higher compared with the two experimentally reported values for the *d*-AlNiCo quasicrystals (see Sec. II D , and Fig. 3). This is most likely due to a partial occupancy of the Al(4) orbit of sites that are fully occupied in our model.

Finally, we note that a recent HRTEM study with an alloy nominal composition $Al_{71}Ni_{14.5}Co_{14.5}$ (Ref. 18) found a mix-

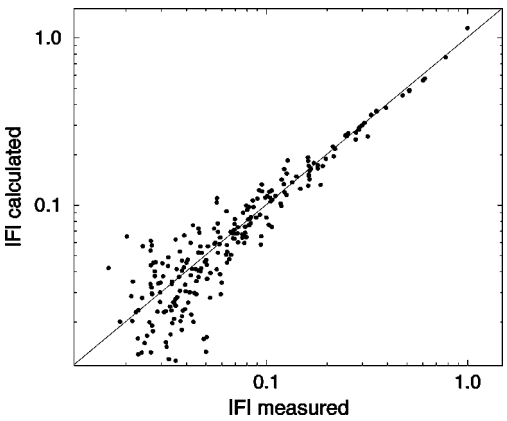

FIG. 2. Log-log plot of the 253 measured and calculated structure factors $|F|$ for the *d*-ANC model.

TABLE I. TM content x, the ''reference'' x_{ref}, atomic density ρ_{at}, relative volume Ω/Ω_{ref} (Ω is the atomic volume used for the calculation, Ω_{ref} is the volume at x_{ref}, see Sec. II C), and valence electron density ρ_{el}, assuming 1.8 valence electrons per TM atom (TM≡Co) for selected Al(Ni,Co) structures used in this study.

Structure	x	x_{ref}	ρ_{at} [Å^{-3}]	Ω/Ω_{ref}	ρ_{el} [Å^{-3}]	Pearson symbol
Al	0.000	0.000	0.0602	1.000	0.181	$cF4$
O-$Al_{13}Co_4$	0.235	0.250	0.0701	0.956	0.191	$oP102$
Al_9Co_2Ni	0.250	0.250	0.0686	0.984	0.185	$oI96$
Al_3Ni	0.250	0.250	0.0687	0.982	0.186	$oP16$
Al_5Co_2	0.286	0.286	0.0726	1.000	0.193	$hP28$
d-ANC	0.291	0.286	0.0724	1.005	0.191	$mP110$

ture of two stable approximant phases termed ''PD_1'' and ''PD_2.'' The underlying geometry of both structures are two different tilings of golden rhombi (with $a\sim 20$ Å edge length) and the PD_2 structure is a superstructure of the model described here: adjacent rhombi alternate between two variant decorations, and the ''periodic'' lattice parameter c is doubled.

B. Crystals

In order to assess the impact of the structural and chemical variations on the dynamical properties of the Al-Co system in the vicinity of the composition of the decagonal quasicrystal, we choose from the Al-(Ni,Co) phase diagram four crystalline phases: Al_3Ni,[19] Al_9Co_2Ni,[20] and O-$Al_{13}Co_4$(Ref. 21) with the TM content $x\sim 0.25$, and Al_5Co_2 at $x\sim 0.29$. Since the pair interactions are in principle sensitive to the variation of x and the atomic density (see Sec. II C), we can only reliably compare the differences in the dynamical properties when these two parameters are fixed; this is nearly exactly the case for the Al_3Ni vs Al_9Co_2Ni at $x=0.25$, and approximately for our d-ANC approximant model (Sec. II A)

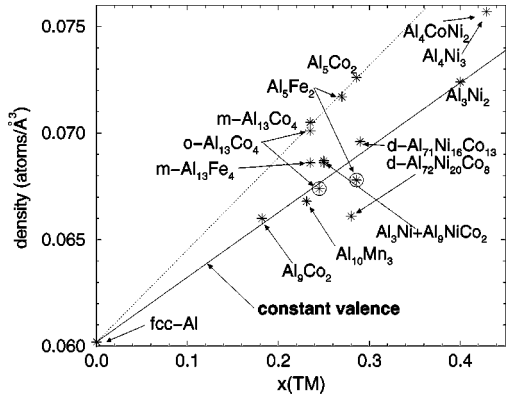

FIG. 3. Atomic density as a function of the TM content in some Al-TM alloys. The valence electron density $\rho_{el}=0.181$ Å^{-3} is constant along the solid line, assuming 1.8 electrons per TM≡Co; the dashed line connects fcc Al with Al_5Co_2. The circled stars denote an alternative plausible choice of the Al fractional occupancy.

vs the Al_5Co_2 structure near $x=0.29$. The O-$Al_{13}Co_4$ structure is closely related to both Al_9Co_2Ni and d-ANC. The basic structural data on these phases are compiled in Table I, and the projected structures are shown in Figs. 1(a)–1(d).

The relationship between O-$Al_{13}Co_4$ and Al_9Co_2Ni is illustrated in Figs. 1(c) and 1(d), showing the structures projected along the pseudodecagonal axis. Perpendicular to this axis, the atoms in O-$Al_{13}Co_4$ are arranged in flat (F) (smaller circles in the figure) layers, alternating with puckered (P) (larger circles) layers, and with mirror planes on the F-layers. Connecting nearest Co atoms in the P layer leads to a tiling of pentagons and skinny rhombi with $\sim 36°$ acute angles (solid lines in the figure). In contrast, the Al_9Co_2Ni repeats a sequence of *six* pseudodecagonal layers: $PFP'F'PF$. The TM atoms in P layers are again located on vertices of the skinny rhombi, but there is only a 3/5 fraction of the pentagon tile. Up to the positions of certain Al atoms, this structure may be viewed as a twinned fragment of the O-$Al_{13}Co_4$ unit-cell motif.

On the other hand, the Co atoms in the F layer of the O-$Al_{13}Co_4$ structure are located approximately at vertex positions [center of pentagons in Fig. 1(c)] of a tiling of squashed hexagons with an edge length of ~ 6.5 Å. The squashed hexagon tile has been proposed as one of the three building units (hexagon, boat, star) for models of the decagonal AlCo and AlCuCo phases.[22,23]

There are several reasons why we included both of these structures into our list despite their structural similarity. First, the Al_9Co_2Ni structure is an ideal candidate for comparison with Al_3Ni, which has neither fractionally occupied sites nor close pairs of atoms. The O-$Al_{13}Co_4$ phase has also no fractional occupancies reported from the diffraction data; however, the presence of a few very short Al-Al bonds (~ 2.3 Å), some large refined Al Debye-Waller factors, as well as energetic considerations[4] suggest that some Al sites might be partially occupied. The phenomenon of partial occupancy and its impact on the vibrational properties deserves special attention and later on we will compare the full-occupancy O-$Al_{13}Co_4$ model with variant models with fractional occupancy of some Al sites.

As our study is entirely based on isotropic pair potentials, the differences between the structures are conveniently represented by the pair distribution functions (PDF) $g(r)$. In Fig. 4, we compare the $g(r)$ of Al_3Ni with that of Al_9Co_2Ni [Fig. 4(a)] and Al_5Co_2 with the model of the d-AlNiCo approximant [Fig. 4(b)].

C. Pair potentials

Recently, Moriarty and Widom[2] developed full GPT interatomic potentials for transition-metal aluminides. The potentials include all sp, sp-d, and d-d interactions within the local density-functional theory, and they select correctly the sequence of stable phases in Al-Co and Al-Ni binary phase diagrams among many Al-TM structures.[4] For a transition-metal content of $x\lesssim 0.3$, the energetics appear to be correctly described by the potentials truncated at the pair-potential level. However, stability of Al_5Co_2 over the Al_5Fe_2 structure

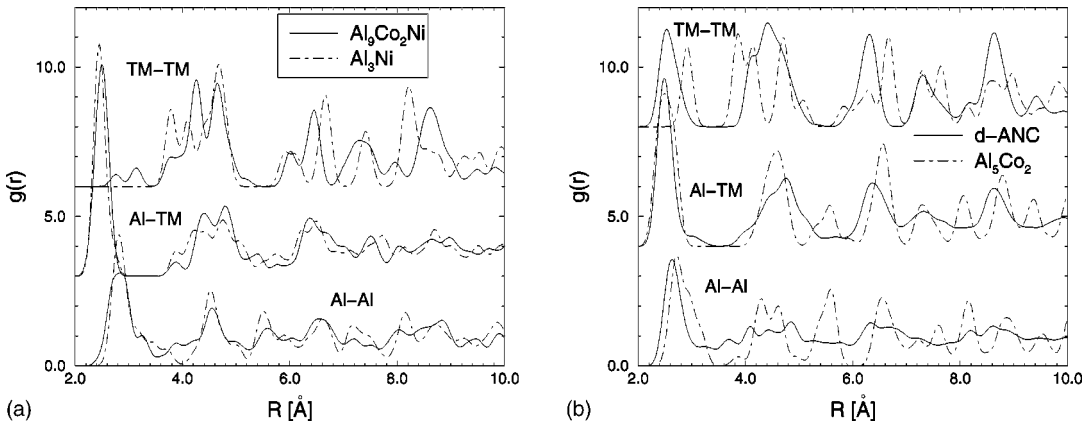

FIG. 4. (a) Comparison of radial distribution functions at $x=0.25$ (Al_9Co_2Ni and Al_3Ni structures) and (b) at $x\sim0.30$ (*d*-ANC model and Al_5Co_2). In the *d*-ANC case, the PDF was taken from the model relaxed under the SE potentials, in the other cases the structures are unrelaxed models based on the diffraction data, in all cases convolved with a gaussian with $\sigma=0.1$ Å.

in the Al-Co system required inclusion of the many-body terms in the pair potentials' expansion.

In our dynamical study, we only consider the pair-potential term in the expansion of the total energy

$$E_p(\mathbf{R}_1,\ldots,\mathbf{R}_N)=\sum_{\mathbf{n}}\sum_{i<j} v_2^{\alpha\beta}(|\mathbf{R}_j-\mathbf{R}_i-\mathbf{n}|;\Omega,x), \quad (1)$$

which depends explicitly on atomic volume Ω and the TM concentration x. Here, $\mathbf{n}$ denote lattice translation vectors, $\mathbf{R}_1\ldots\mathbf{R}_N$ are the positions of N atoms within the unit cell, and $\alpha\beta$ stands for the Al-Al, Al-TM, or TM-TM pairs of atoms. It turns out that for the sequence of atomic volumes experimentally observed in stable Al-Co phases with $x\lesssim0.3$, the x and Ω dependence is nearly accurately canceled, so that the pair potentials have no apparent dependence on x (while the cohesive energies are significantly shifted by the volume-energy term, which *is* strongly x dependent). Thus, for the limited set of compositions x_{ref} and atomic volumes Ω_{ref} at which the GPT potentials were evaluated, it is plausible to use a single set of $x=0$ potentials at the reference volumes and TM concentrations. We show the $x=0$ set of the potentials from Ref. 2 in Fig. 5 (Al-Al) and Fig. 6 (Al-Co and Co-Co).

Our study focuses at $x=0.25$ and $x\sim0.29$, and we used uniformly the *experimental* atomic volumes Ω determined from the diffraction data. Our Ω departs appreciably from Ω_{ref} (see the fifth column in the Table I) only in the case of the full-occupancy model of O-$Al_{13}Co_4$, in which case we performed additional calculations to investigate the dependence of the vibrational properties on the atomic volume via Al/vacancy substitution or a rescaling of the lattice parameters. Two structures in our list (full-occupancy O-$Al_{13}Co_4$ and the *d*-ANC model) occurred at $x\neq x_{ref}$; in these cases, we evaluated Ω_{ref} assuming valence electron density $\rho_{el}(x_{ref})$ and $Z_{TM}=1.8$.

One problem caused by the truncation of the GPT potentials at the pair-potential level is the deep well in the Co-Co potential at an unphysically short 1.8 Å separation as a result of the direct *d*-*d* interaction between Co atoms. This spurious feature was attributed to the lack of the many-body terms in the potential energy expansion.[4] While we still use GPT potentials for Al_5Co_2, in which case the neighboring Co atoms do not move unphysically close to each other upon relaxation of their positions, in the *d*-ANC case the spurious Co-Co well has a fatal impact on the rings of neighboring Co atoms, and we excluded *d*-ANC from the list of structures studied under the GPT potentials.

Parallel to the GPT potentials, we also used the semi-empirical (SE) Al-Co potentials of Phillips *et al.*[1] (Figs. 5 and 6). The potentials depend on a set of parameters that were determined either from experimental data or *ab initio* simulations. These potentials neglect the direct *d*-*d* interactions (although the *d*-*d* interactions mediated by the electron sea are included), and they are supposed to be valid at a constant valence electron density of fcc Al. The neglect of the direct *d*-*d* interaction leads to a Co-Co pair potential with a plausible position of the first-neighbor well, so that these potentials may be tentatively used also for the structures with neighboring Co atoms. In particular, the *d*-ANC model was only studied with the SE potentials.

In the calculations, we truncated the GPT potentials using

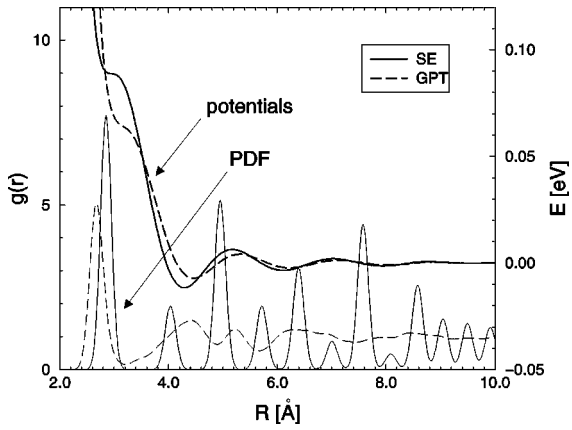

FIG. 5. Radial distribution functions (convolved with a Gaussian with half width $\sigma=0.1$ Å) and two sets of Al-Al pair potentials. The energy scale for the potentials is displayed on the right side. For the GPT potential, the structure is fcc Al; for the SE potential it is an amorphous phase resulting from the MD annealing.

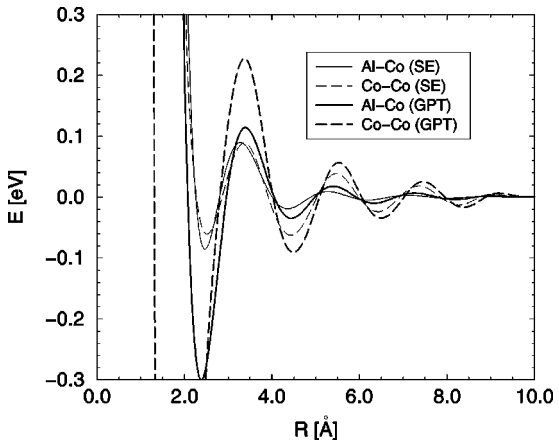

FIG. 6. SE and GPT Al-Co and Co-Co pair potentials.

an interaction cutoff radius $r_{cut}=10$ Å. With the same interaction cutoff the SE potentials exhibit a strong tendency towards phonon instability. The stability was significantly improved when we considered $r_{cut}=7$ Å in this case, and we adopted this cutoff radius for the SE potentials.

D. Atomic density and partial occupancy

The interatomic potentials are a function of the atomic density ρ (or conversely, of atomic volume $\Omega=\rho^{-1}$) and the mean number of valence electrons per atom Z (see Sec. II C); therefore, the atomic density is an important input parameter for our calculations. For crystals with no partial occupancies and chemical disorder, ρ and x are given straightforwardly. However, the partial occupancy appears to be a common phenomenon among stable Al-rich Al-TM phases and presents a substantial problem for the determination of quasicrystal structures lacking translational symmetry.

In Fig. 3, we plot the atomic density ρ as a function of the TM concentration x for selected Al-TM phases up to $x\sim0.4$. The global, approximately linearly increasing trend of $\rho(x)$ suggests that the existing phases have an approximately constant valence electron density over a wide range of the TM concentrations, while the Al valence $Z_{Al}=3$ is larger than the TM valence Z_{TM} (in fact, according to the GPT the TM valence is a function of x).

The dotted line passing through fcc Al and Al_5Co_2 data points in the figure marks a trend for ''dense'' structures. The solid line was calculated assuming a constant valence of fcc Al and $Z_{TM}\equiv Z_{Co}=1.8$ after Ref. 2; it turns out that this line marks a trend for ''loose'' structures. Interestingly, in the case of orthorhombic Al_5Fe_2 (Ref. 19) and O-$Al_{13}Co_4$, their diffraction-data-derived structures match the $\rho(x)$ dependence of the ''dense'' structures. However, from the structural relationship with Al_9Co_2Ni (and according to the energetic considerations in Ref. 4), the optimal O-$Al_{13}Co_4$ model has at least four vacancies and becomes a ''loose'' structure (circled star in the figure). Similarly, a model of Al_5Fe_2 avoiding short Al-Al bonds [by assigning fractional occupancy 0.5 instead 0.7 to the Al(1) site] is also ''loose,'' with $x=0.286$ (circled star). The ''dense'' structure of Al_5Co_2 at the same x has also its ''loose'' counterpart—the $Al_{10}Mn_3$ (Ref. 24) structure in the Al-Mn system, in which one TM site in the Al_5Co_2 structure is vacant.

Finally, we also plotted the measured atomic densities for two slightly different compositions of the Ni-richer *d*-AlNiCo quasicrystal: $Al_{71}Ni_{16}Co_{13}$ (Ref. 25) and $Al_{72}Ni_{20}Co_8$.[26] While the density of the former composition falls slightly above the ''loose'' line, the measured density of the composition of the ''perfect'' (so-called ''Ni-rich basic'' phase) quasicrystal is extremely low and has no counterpart among the structures in Fig. 3.

III. ATOMIC DYNAMICS

A. Harmonic analysis

In the harmonic approximation, the atomic vibrations of the periodic system with N atoms in the unit cell are governed by the equations of motion

$$\omega^2(\mathbf{k})u_{j\nu}=\sum_{j'\nu'}\frac{u_{j'\nu'}}{\sqrt{M_jM_{j'}}}\sum_{\mathbf{n}}e^{-i\mathbf{k}.\mathbf{n}}\frac{\partial^2E_p(\mathbf{R}_1,\ldots,\mathbf{R}_N)}{\partial u_{j\nu}\partial u_{j'\nu'}}, \tag{2}$$

where ω is the frequency, $u_{j\nu}$ is the νth component of the displacement, and M_j is the mass of an atom j. The second summation is through translation vectors $\mathbf{n}$ to include the contributions from all atoms within an interaction radius for a wave vector $\mathbf{k}$ from within the first Brillouin zone.

We solved the standard eigenvalue problem represented by Eq. (2) using the LAPACK library routine ZHEEV for a mesh of $\mathbf{k}$ points inside the first Brillouin zone to obtain $3N$ real eigenvalues $\omega_i^2(\mathbf{k})$ (these are positive for a stable structure) and for each of these the corresponding normalized eigenvectors $\mathbf{u}_{ij}(\mathbf{k})$ with three complex components for an atom j. The phonon density of states (DOS) may then be evaluated for any subset of sites α in the structure from the statistics of eigenfrequencies

$$D_\alpha(\omega)=\frac{1}{3N_\alpha N_{\mathbf{k}}}\sum_{i=\alpha,\mathbf{k}}w_i\delta(\omega_i(\mathbf{k})-\omega), \tag{3}$$

where $w_i=\Sigma_{j=\alpha}\mathbf{u}_{ij}\mathbf{u}_{ij}^{\star}$ is the total squared eigenvector amplitude on the atoms α in the ith mode, N_α is the total number of sites α, $N_{\mathbf{k}}$ the number of $\mathbf{k}$ points, and δ denotes a resolution function; our choice was to use a gaussian $(\sigma\sqrt{2\pi})^{-1}\exp[-\frac{1}{2}((\omega_i(\mathbf{k})-\omega)/\sigma)^2]$, with $\sigma\sim0.5$ meV. For comparison with the experimental ''generalized'' vibrational density of states (GVDOS) defined by Eq. (4), the latter has the instrumental resolution of about 0.5 meV in the low-energy part of the spectrum, degrading by an order of magnitude at the high-energy end of the spectrum. The GVDOS is a weighted sum of the elemental partial density of states

$$G(\omega)=\sum_\alpha e^{-2W_\alpha}\frac{\sigma_\alpha c_\alpha}{M_\alpha}D_\alpha(\omega), \tag{4}$$

where M is the mass, σ the total neutron cross section, and c the concentration of the element α. The Debye-Waller factor

$$W_\alpha = \frac{\hbar^2 |\mathbf{q}|^2}{2M_\alpha} (3N_\alpha N_{\mathbf{k}})^{-1} \sum_{i,\mathbf{k}} w_i \frac{n(T,\omega_i(\mathbf{k})) + \frac{1}{2}}{\omega_i(\mathbf{k})} \quad (5)$$

is temperature dependent via the Bose-Einstein thermal occupation function $n(T,\omega)$, and $|\mathbf{q}|$ is the momentum transfer. (Notice that except in Eq. (4), label α generalizes to any subset of the topologically equivalent sites.] The Debye-Waller (DW) factors calculated from Eq. (5) are directly comparable to the isotropic ''crystallographic'' DW factors from the diffraction refinements,

$$B_\alpha = 16\pi^2 \frac{W_\alpha}{|\mathbf{q}|^2}, \quad (6)$$

where W_α denotes the DW factor of the atom α.

An eigenmode ω_i is characterized by its *participation ratio*

$$P_i = \frac{\left(\sum_j \left| \mathbf{u}_{ij} \right|^2 \right)^2}{N_{at} \sum_j (|\mathbf{u}_{ij}|^2)^2}, \quad (7)$$

where the index j goes through N_{at} atoms in the unit cell. The definition of P_i provides a quantitative measure of the localization: $P_i \to N_{at}^{-1}$ when there is a single atom j with nonzero displacement $\mathbf{u}_{ij}$, and $P_i \to 1$ when the displacements of all atoms have an equal (nonzero) amplitude. A subtlety in the definition of the P_i is the neglect of the phase factor in the $|\mathbf{u}_{ij}|^2$. However, for crystals with large unit cells, all the relevant information may be obtained from the Γ point $\mathbf{k}=0$, in which case all eigenvectors and the displacements are real.

A related quantity called the *phase quotient* has been proposed to characterize the correlation between eigenvectors of the neighboring atoms for disordered materials[27]

$$Q_i = \frac{\sum_{jj'} \mathbf{u}_{ij} \cdot \mathbf{u}_{ij'}}{\sum_{jj'} |\mathbf{u}_{ij} \cdot \mathbf{u}_{ij'}|}, \quad (8)$$

where the sum jj' denotes all nearest-neighbor interatomic bonds. $Q_i \to 1$ for the acoustic modes and $Q_i \to -1$ for optic modes with a phase shift of π on the neighboring atoms.

B. Molecular-dynamics simulation

We employed the standard Verlet algorithm in a microcanonical (number density)×velocity×time ensemble. Typically, we took supercells with about 400 atoms in the periodic cell, and used two different molecular-dynamics (MD) schedules aimed at different goals.

1. Temperature dependence of the DW factor

Here, we cooled from $T=300$ down to 50 K in 50-K steps, with 500-ps equilibration time at each temperature and consecutive 500-ps measurement time (time step $\Delta t = 10^{-14}$ s). For each individual atom j, we took the time averages $\langle u_{j\nu}^2 \rangle - \langle u_{j\nu} \rangle^2$, where ν denotes Cartesian coordinates. These were then averaged over all atoms of a given type α to obtain the ''crystallographic'' Debye-Waller factor

$$B_\alpha^{MD} = \frac{8\pi^2}{3N_\alpha} \sum_{j=\alpha} \langle u_{j\nu}^2 \rangle - \langle u_{j\nu} \rangle^2, \quad (9)$$

where the summation j' is through the atoms α. The formula is only valid in the absence of diffusion. Some large values of the DW factors even at room temperature are due to a subset of Al atoms, for which Eq. (9) is not valid.

The B^{MD} can be compared directly with B defined by Eqs. (5) and (6) in the *classical* high-temperature approximation, in which

$$n(T,\omega) + \frac{1}{2} = \exp\left(\frac{k_B T}{\hbar\omega} - 1 \right)^{-1} + \frac{1}{2} \approx \frac{k_B T}{\hbar\omega}. \quad (10)$$

2. High-temperature stability and atomic configurations

We reduced the time step by a factor 2, and after the 100-ps equilibration period we recorded 500 atomic configurations in 1-ps time intervals. The configurations were used to obtain the projected density maps.

IV. RESULTS

A. Stability

Prior to diagonalizing the dynamical matrix, the atoms must be relaxed into their equilibrium positions with respect to the interatomic forces. Owing to their high symmetry, the mechanical stability of simple structures with few atoms per unit cell is robust with respect to the variation of the interatomic forces. Complex structures, on the contrary, are sensitive to the detailed shape of the interatomic potentials and to their oscillating tails. In all structures studied here, the equilibration of the atomic forces using relaxation at $T=0$ K introduced small atomic displacements, but did not disturb the topological ordering of atoms. The main stabilizing factor is the rigidity of the subnetwork of Co atoms, arising from (i) their uniform distribution in the Al matrix (at the same time, the Al-Co pair potential has a deep well at the nearest-neighbor distance) and (ii) the fact that the Co-Co potential exhibits a strongly oscillating tail, correlating the Co atom positions far beyond the second-neighbor shells. All structures listed in Table I achieved mechanical stability such that the atomic positions correspondeded to the minimum of $E_p(\mathbf{R}_1 \ldots \mathbf{R}_N)$ within the machine precision.

In the case of the SE potentials, despite their mechanical stability, two structures (Al_5Co_2 and *d*-ANC) exhibited few imaginary eigenfrequencies. Additional relaxation procedures were needed to avoid the instability: we took supercells containing a few images of the unit cell (see column ''note'' in Table II) and performed the MD annealing at a finite temperature followed by a conjugate gradient relaxation of the atomic positions. This treatment introduced an additional displacive modulation due to the translational symmetry breaking and decreased the pair-potential energy

TABLE II. Transverse, longitudinal, and mean sound velocities for the selected Al(Co,Ni) structures in $ms^{-1}\times10^3$, using SE and GPT pair potentials. The anisotropy is reported as $\pm(v_{max}\text{-}v_{min})/2$. Symbol ''UC'' in the column ''note'' indicates the number of the images of the unit cell in a supercell used for calculation. Alternatively, the column reports variant Al occupation models relative to the full-occupancy models (the case of O-$Al_{13}Co_4$).

SE	v_T	v_L	v_s	Note	Ω/Ω_{ref}
amorphous Al	2.36±0.28	5.59±0.11	2.66	UC×64	
O-$Al_{13}Co_4$	3.57±0.13	6.28±0.07	3.97		0.956
	3.47±0.15	6.12±0.39	3.86	−6 Al	1.023
	3.87±0.30	7.17±0.26	4.32		0.914
Al_9Co_2Ni	3.62±0.23	6.07±0.33	4.01		
Al_3Ni	3.48±1.39	5.64±1.57	3.84		
Al_5Co_2	3.35±0.36	4.92±0.47	3.65	UC×8	
d-ANC	3.80±0.23	6.57±0.25	4.21	UC×4	
GPT					
fcc Al	3.64±0.15	6.89±0.10	4.06		
O-$Al_{13}Co_4$	4.21±0.20	7.96±0.74	4.96		0.956
	4.19±0.26	7.86±0.60	4.69	−6 Al	1.023
	3.56±0.21	6.42±0.21	3.96	−6 Al	1.048
Al_9Co_2Ni	4.77±0.65	8.20±0.35	5.14		
Al_3Ni	4.98±0.35	7.67±1.17	5.41		
Al_5Co_2	3.67±1.92	6.57±2.30	4.08		

marginally by 0.2 meV/atom for Al_5Co_2 structure and appreciably by ~10 meV/atom per atom for *d*-ANC. Thus such a displacive modulation may become a nonnegligible factor favoring the complex structures.

B. Pure aluminum limit

In this limit, we find a fundamental deviation of the SE Al-Al potential from the expected behavior. Although the fcc Al structure, due to its high symmetry, does not exhibit any relaxation displacements at $T=0$ K, MD annealing at a finite temperature of a supercell model with 256 atoms in the supercell leads to a phase transformation to an *amorphous phase*, with the structural energy decreased by ~60 meV/atom relative to fcc Al. In Fig. 5, we plot the Al-Al potential together with the fcc Al pair-distance histogram and the pair distribution function of the relaxed supercell model.

Comparison of the two sets of potentials at the nearest-neighbor distance shows that while in the case of the GPT potentials the interaction is strongly repulsive, in the SE case the interaction is almost neutral, due to the shelflike feature in the potential. The lack of nearest-neighbor repulsion is the reason of the instability in fcc Al: the potential well near 4.5 Å is filled by distorting the bonds at 4.05 and 4.96 Å, at the price of shrinking the nearest-neighbor bond at 2.86 Å. (A realistic phonon spectrum is obtained when we scale the fcc Al unit-cell volume by a factor of 0.96^3 to ~0.89.) Part of the reason for the improved stability at higher *x* content is the fact that the pair potentials remain approximately invariant, while the volume per atom shrinks as *x* increases; consequently, the nearest-neighbor Al-Al bonds eventually fall on the repulsive shoulder of the potential, constraining the motion of the Al atom.

C. Vibrational properties: Structural trends

In Fig. 7 we show the phonon DOS calculated via Eq. (3) for the two sets of interactions (SE and GPT). The complex dynamical matrix was diagonalized on a mesh of points inside the Brillouin zone giving a total of about 6×10^4 eigenvalues for each structure. We evaluated the sound velocities (Table II) from the three smallest eigenvalues of the dynamical matrix near the Γ point of the Brillouin zone, with $|\mathbf{k}|=10^{-2}$ Å pointing along the directions of the reciprocal-lattice vectors and averaging over the three directions (we assigned the two smallest eigenvalues to the transverse modes and the third to the longitudinal). In the long-wavelength (acoustic) limit, the phonon DOS $D(\omega)$ is related to the mean sound velocity v_s by Eq. (12) in Sec. IV F. Finally, Table III shows the Debye-Waller factors [Eq. (6)]. For comparison, we compiled the Debye-Waller factors for some Al-rich aluminides available in the literature (Table IV).

The phonon DOS of Al_3Ni on one hand and of Al_9Co_2Ni on the other contrasts the dynamical behavior of simple and complex structures: the DOS of Al_9Co_2Ni shows excess states at both the low- and high-energy edges of the spectrum. The excess (nonacoustic) low-energy states result in higher values of the Debye-Waller factor [due to the $1/\omega$

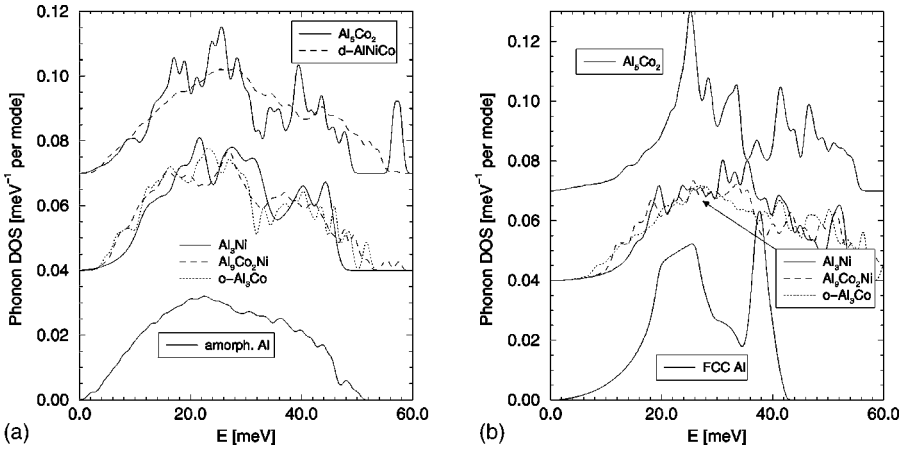

FIG. 7. Phonon DOS of the Al_5Co_2, Al_3Ni, Al_9Co_2Ni, O-$Al_{13}Co_4$, and the *d*-ANC model for the two sets of potentials: (a) SE and (b) GPT.

TABLE III. Isotropic Debye-Waller factors B of Al and TM in Å^2, calculated from Eq. (6) under the SE and GPT potentials.

	Note	SE		GPT	
		B_{Al}	B_{TM}	B_{Al}	B_{TM}
Al		2.47		0.69	
O-$Al_{13}Co_4$		1.05	0.46	0.54	0.32
	-6Al	1.03	0.50	0.54	0.32
	adjusted	0.78	0.39	0.64	0.42
Al_9Co_2Ni		1.01	0.44	0.54	0.28
Al_3Ni		0.78	0.48	0.49	0.27
Al_5Co_2		0.95	0.47	0.54	0.38
d-ANC		0.92	0.42		

TABLE IV. Isotropic crystallographic Debye-Waller factors for some aluminides at room temperature from diffraction refinements (we averaged Wyckoff site B factors over atomic species).

Structure	B_{Al} [Å^2]	B_{TM} [Å^2]	Reference source
O-$Al_{13}Co_4$	1.21	0.88	21
Al_9Co_2Ni	1.41	1.03	20
$Al_{10}Mn_3$	1.01	0.67	24
Al_5Co_2	0.71	0.43	24
$Al_{13}Fe_4$	0.94	0.75	34
$Al_{13}(CoRh)_4$	1.0	0.62	35
fcc Al	0.90		36

factor in Eq. (5)]. The character of these low–energy states is discussed in Sec. IV F. There is no marked difference between the spectra of O-$Al_{13}Co_4$ and Al_9Co_2Ni, except that the latter is more structured, as expected due to the higher symmetry of the structure.

A similar comparison between Al_5Co_2 and d-ANC at higher x content is hampered by the anomalous dynamical properties of Al_5Co_2 for both sets of potentials. For the SE potentials with a short interaction cutoff radius $r_{cut}=7$ Å, the DOS exhibits a soft transverse mode (a bump near 9 meV in Fig. 7) that develops into an instability at $r_{cut}=10$ Å. For the GPT potentials at $r_{cut}=10$ Å, the sound velocities also exhibit a strong anisotropy and soft modes, indicating closeness of the instability (the smallest transverse sound velocity was only 1290 ms^{-1}).

The sound velocities were experimentally determined for decagonal AlNiCo from the phonon dispersion (Ref. 7) and acoustic spectroscopy (Ref. 25), yielding consistently $v_T \sim 4100$–4600 and $v_L \sim 7000$ ms^{-1}. As can be seen in Table II, these numbers are overestimated by the GPT potentials (particularly the longitudinal sound) and underestimated by the SE potentials. A separate confirmation of this trend for the two sets of potentials is provided by the comparison of the $T=300$ K Debye-Waller factors calculated from the dynamical matrix (Table III) and obtained from the diffraction refinements (Table IV): the GPT potentials underestimate both the Al and TM Debye-Waller factors, while SE potentials appear to slightly overestimate B_{Al} and underestimate B_{TM}. However, we point out that the B factors fitted from the diffraction data should be considered, at least for the complex structures, as an *upper-bound* estimate, due to the coupling between partial occupancy and the thermal vibration of an atom about the equilibrium position in the diffraction-data fits. On the other hand, the B factors evaluated here are more likely the *lower* bound, since we (i) allow only for limited relaxations of the complex structures (see the discussion of the stability in Sec. IV A), and (ii) we use the phonon spectrum calculated at $T=0$ K with the $T=300$-K thermal occupation factor. In fact, the room-temperature molecular-dynamics simulation discussed in Sec. IV H leads to increased partial B_{Al} factors, while the B_{TM} is consistent with the dynamical-matrix calculation.

D. Partial Al and TM phonon DOS

We consistently find for the set of structures considered here and the two sets of pair potentials the same gross features of the partial Al and Co density of states (Fig. 8): the Al band is broad and extends up to about 60 meV, while the TM band exhibits a rather sharp maximum below 30 meV. This leads to a GVDOS that correctly explains the difference between the experimentally determined phonon GVDOS of d-ANC and O-$Al_{13}Co_4$ (see Sec. IV E).

However, apart from this gross similarity given by the atomic interactions rather than by the atomic structure, there

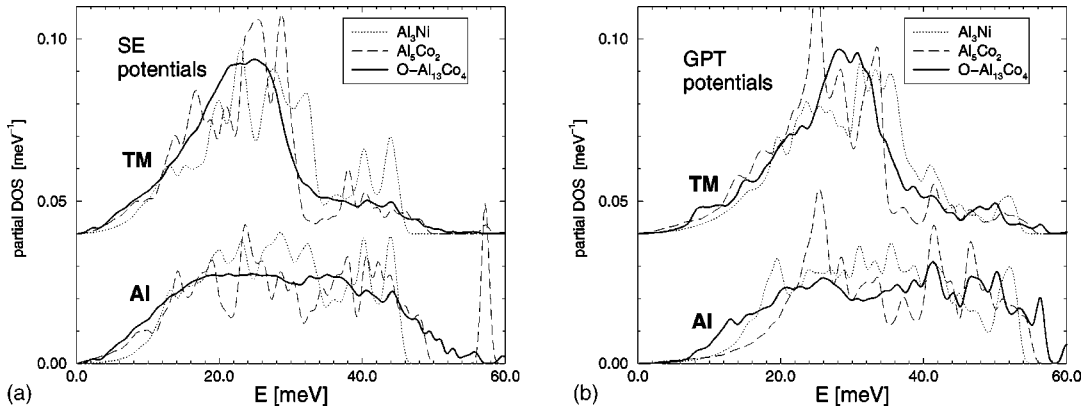

FIG. 8. Partial aluminum and TM phonon DOS: (a) SE potentials and (b) GPT potentials.

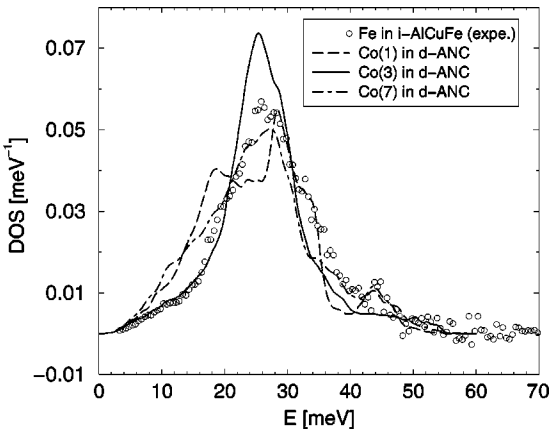

FIG. 9. Partial Fe phonon DOS in *i*-AlCuFe determined [explained in Fig. 1(e)].

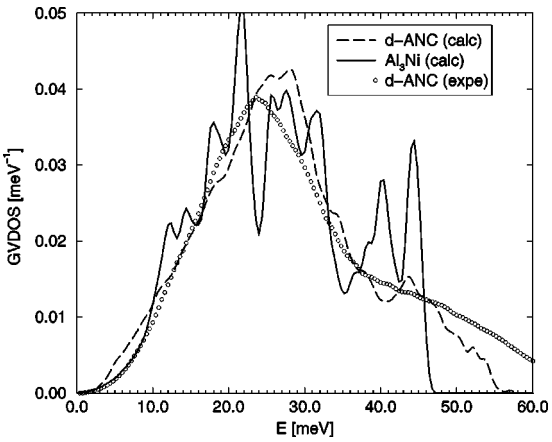

FIG. 10. Experimentally determined GVDOS of $Al_{70}Ni_{15}Co_{15}$ and calculated GVDOS of *d*-ANC approximant model and Al_3Ni crystal (SE potentials).

is one apparent difference in the contrast between the Al and TM partial DOS Al_3Ni and O-$Al_{13}Co_4$: while in the former case the partial DOS shares many details in common (features appearing in the Al partial occur also in the TM partial DOS at the same energy), the wiggles in the Al and TM partials lose most of the correlation in the case of O-$Al_{13}Co_4$. This difference is due to the fundamentally different character of the phonon eigenstates in the simple and complex structures (see discussion in Sec. IV F); they are extended throughout the energy spectrum in Al_3Ni and are more localized in O-$Al_{13}Co_4$, with enhanced localization near both the low- and high-energy ends of the spectrum.

Our calculated TM partial phonon DOS may be qualitatively compared to the recently measured partial DOS of Fe in *i*-AlCuFe.[28] Albeit the decagonal and icosahedral structures are different, we conjecture that due to the localization, the shape of the TM partial DOS is well described as an average over the *local* DOS on the Fe atoms and therefore is not sensitive to the detailed structure. Secondly, the GPT predicts that the Al-TM interactions are very similar for Co, Ni, and Fe (Fig. 8 in Ref. 2). Figure 9 shows the partial Fe DOS compared to the local DOS on the three TM sites occuring in our *d*-ANC model presented in Figs. 1(e) and (f). These are labeled Co(1) (atoms in the central column of the decagonal cluster, each having four neighboring TM atoms), Co(3) (with *no* TM neighbors), and Co(7) (with a single TM neighbor). The effect of the neighboring TM atom is apparent: for a single neighbor, the DOS clearly splits and for more neighbors it further broadens. The Debye-Waller factor B is lowest for the Co(3) site (~ 0.37 Å^2) and is some 15% higher for the other two Co sites (~ 0.43 Å^2). The Fe partial exhibits striking resemblance to the Co(3) DOS in *d*-ANC with no TM neighbors; this is plausible in view of the low Fe content in *i*-AlCuFe ($\sim 12\%$). (We speculate that the Cu atom is acting approximately as an average Al/Co atom, as suggested by the succesfull mock-ternary model of *d*-AlCuCo.[23])

E. Comparison with experimental GVDOS

The experimental GVDOS of decagonal $Al_{70}Co_{15}Ni_{15}$ (Ref. 29) and the calculated (using SE potentials) GVDOS of the *d*-ANC approximant are compared in Fig. 10. The character of the GVDOS is determined by a broad structureless Al band extending up to 60 meV and by a much sharper TM band peaking at about 29 meV. The position of the main peak in the experimental spectrum can be clearly attributed to the TM partial.[29] This peak is located at about 24 meV in the experimental GVDOS.

In the low-energy part of the spectrum, the calculated GVDOS is higher than the experimental—despite the fact, that even the experimental GVDOS has a significant excess of states in this part of the spectrum (see the discussion in Sec. IV F and our preliminary study in Ref. 15) over the expected acoustic contribution derived from the experimental mean sound velocity. In both spectra, this excess is due to the localized low-energy modes.

In the figure, we also superimposed the calculated GVDOS of the Al_3Ni structure (SE potentials). Accidentally, the experimental GVDOS of *d*-ANC and the calculated GVDOS of Al_3Ni are in miraculous agreement up to at least 9 meV. This indirectly suggests the idea that the *amount* of the low-energy modes in quasicrystals—with prevalence of the localized modes over the acoustic—somehow correspond to soft modes occurring in crystalline systems with similar composition. The soft mode in Al_3Ni occurs for $\mathbf{k}$ along the (1,1,0) direction with $v_T(1,1,0)=1720$ ms^{-1}, while for the stiffest transverse mode $v_T(0,1,0)=4360$ ms^{-1}.

Figure 11 shows experimental[30] and calculated GVDOS of O-$Al_{13}Co_4$ for the two sets of atomic interactions. We considered two variant structural models, both at the experimental volume: a full-occupancy 102-atom model and a 96-atom model with six Al sites vacant. In the former case, the atomic volume is shrinked by a factor of 0.956 relative to the required volume at which the potentials were evaluated; in the 96-atom model, the atomic volume is expanded by a factor of 1.023 (see Table I). Apparently, this $\sim 7\%$ variation of the atomic volume does not change the GVDOS much at the fixed dimensions of the unit cell.

We also attempted to match the experimental GVDOS by varying the unit-cell dimensions (and considering the full- or fractional-occupancy models). The results are shown in the

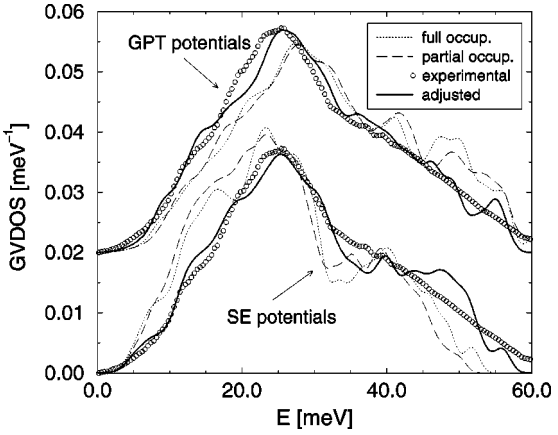

FIG. 11. GVDOS of O-$Al_{13}Co_4$ with full occupancy (102 atoms in the unit cell) and with six Al→vacancy substitutions for the two sets of the potentials. The data are compared to the experimentally determined phonon GVDOS of O-$Al_{13}Co_4$ at $T=300$ K. The ''adjusted'' GVDOS was calculated at variant atomic volume for the 102-atom (SE potentials) and 96-atom models (GPT).

same figure as a solid line and denoted as ''adjusted.'' For the SE potentials, we used the model with full occupancy and scaled the unit cell uniformly by a factor of 0.985[3]. For the GPT potentials, the best fit was obtained using the 96-atom model, with an anisotropic scaling factor (0.97, 1.02, 1.035) for the ''periodic'' and the two pseudodecagonal unit-cell dimensions, respectively. (We noticed that the shrinking of the ''periodic'' direction lattice parameter c is crucial for maintaining the stability at increased lattice parameters a and b in the pseudodecagonal plane.) The effect of these variations on the sound velocity is summarized in Table II; for both SE and GPT interactions, they approach more closely the experimentally measured values in d-ANC.

The effect of scaling the volume of the unit cell vs the variation of the fractional occupancy can be most readily deduced from the SE potential data in Table II (for the GPT potentials we scaled the unit-cell volume anisotropically to avoid instability). Removing six Al atoms increases the relative atomic volume Ω/Ω_{ref} by nearly 7%, while the mean sound velocity softens by only 3%. On the other hand, when the unit cell is uniformly shrunk for the full-occupancy model by 4.5%, the mean sound velocity hardens by nearly 9%.

F. Nonacoustic excitations at low energies

The experimental search for the vibrational properties generic or specific to quasicrystals has in the past focused on the character of the acoustic branches.[6,7] However, it is only recently that there has been increasing evidence for nonacoustic low-energy states that show up in the phonon DOS (Refs. 15 and 28, in excess heat capacity[11] or in an atypical low-temperature variation of the sound velocity.[12–14] On the theoretical side, the low-energy localized (confined) states with extremely low participation ratios have been found in the i-AlZnMg quasicrystal.[31] The eigenmode analysis revealed that the corresponding modes localize on special topologically frustrated sites with coordination $Z=13$ that are

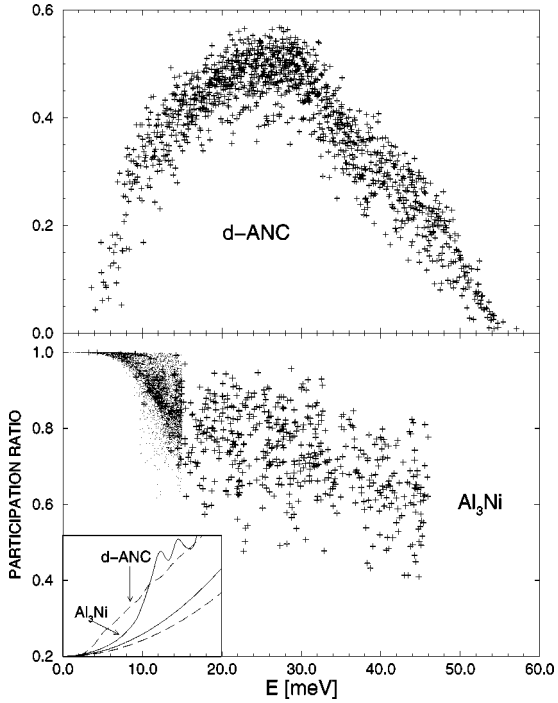

FIG. 12. Participation ratio of the d-ANC model and the Al_3Ni structure (SE potentials). For clarity, $P(\omega)$ is calculated only for the Γ point (d-ANC) and 12 k points (Al_3Ni) (plus symbols). For the low-energy part of Al_3Ni, $P(\omega)$ is shown as dots for a densely sampled Brillouin zone. The inset shows the corresponding phonon DOS. The parabolas below the DOS curves marked by arrows are the corresponding ''Debye DOS'' calculated from the sound velocities v_s.

characterized by a high density of disclination lines.[32] i-AlZnMg belongs to the Frank-Kasper family of quasicrystals with nearly close-packed structure. The complex structures of Al-rich aluminides are rather characterized by ''open'' local environments, providing in general a much stronger support for the localization of the low-energy vibrations.

In the following we demonstrate how the character of an eigenstate depends on the structure, focusing on the low–energy part of the spectrum. As an illustrative example, we compare the d-ANC model with the Al_3Ni structure (SE potentials), as in Sec. IV E. The appropriate quantity revealing the character of the eigenmodes is the participation ratio P_i defined for each eigenmode ω_i [Eq. (7)].

For the (relatively) simple structure of Al_3Ni, the modes are purely extended up to about 5 meV, then they start to localize gradually, with the mean $P(\omega)$ decreasing approximately linearly down to ~ 0.6 near the high-energy end of the spectrum (Fig. 12, bottom panel). A completely different picture emerges for the model of the d-ANC structure (Fig. 12, top panel): $P(\omega)$ falls off very quickly down to extremely low values already near 3–4 meV (this is not evident from the figure, where we only display P at the Γ point), then the mean $P(\omega)$ starts to increase again to its local maximum near the center of the spectrum [$P(\omega)\sim 0.5$], to fall off again down to nearly zero at the high-energy end of the spectrum. However, a feature common to both models is that

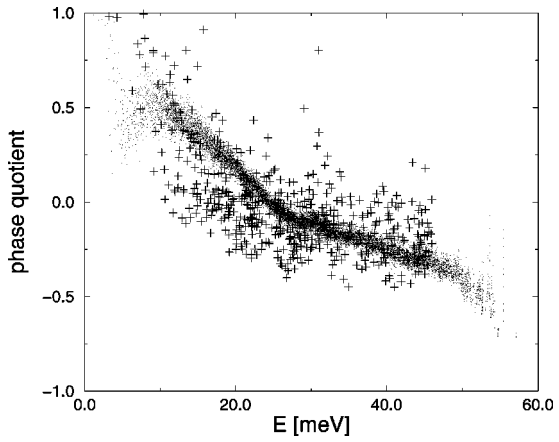

FIG. 13. Phase quotient of the *d*-ANC model (dots) and the Al_3Ni structure (plus symbols) for SE potentials.

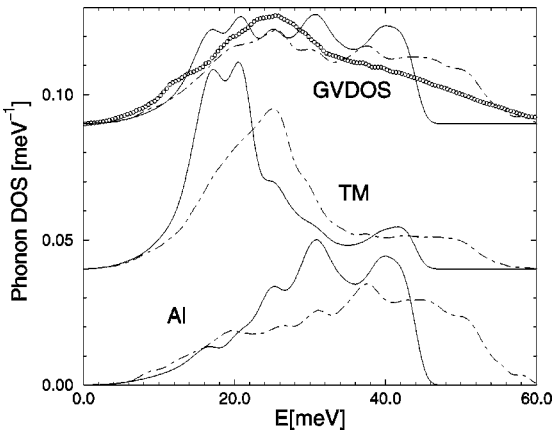

FIG. 14. Al partial phonon DOS (bottom), TM partial DOS, and GVDOS (top) for two simple spring models (solid and dot-dashed line). Circles are the experimentally determined GVDOS of O-$Al_{13}Co_4$.

$P(\omega)$ actually behaves as a function: although there is always a spread among the P_i's at a given ω, there is never more than one characteristic $P(\omega)$. This indicates that the DOS $D(\omega)$ corresponds to the ''mixed'' states with more or less unique $P(\omega)$, rather than to a superposition of purely extended and purely localized modes.

A similar trend is found for the phase quotient $Q(\omega)$ (Fig. 13) defined by Eq. (8). For both *d*-ANC and Al_3Ni, the phases there have a threshold energy of about 25 meV; below this energy, the neighboring atoms tend to vibrate in phase and above with opposite phase, with extreme values of $Q(\omega)$ at the ends of the energy spectrum. Apart from the anomaly in the case of *d*-ANC at low energies that can apparently be related to the low-energy localized states, the ω dependence of Q is surprisingly regular; more precisely, it appears there are two well-defined slopes above and below the threshold energy.

The localized low-energy excitations provide a tentative explanation of the discrepancy between the neutron GVDOS (Ref. 29) and dispersion-relation measurements[7] in *d*-AlNiCo. The mean sound velocity v_s defined as

$$\frac{3}{v_s^3}=\frac{2}{v_T^3}+\frac{1}{v_L^3}, \tag{11}$$

where v_T and v_L are the transverse and the longitudinal sound velocities, respectively, gives rise to the acoustic contribution to the phonon DOS in the long-wavelength limit

$$\rho D(\omega)=\frac{\omega^2}{2\pi^2 v_s^3}+\beta\omega^4+\ldots, \tag{12}$$

where ρ is the atomic point density, and the coefficient β reflects the cubic nonlinearity of the dispersion relation. From the phonon dispersion,[7] $v_s \sim 4.9\times10^3$ ms^{-1}; however, fitting the experimental GVDOS to Eq. (12) results in $v_s \sim 3.1\times10^3$ ms^{-1} (we find that at low energies, the difference between the GVDOS and the DOS is at most 10%) and $\beta = 2.25\times10^{-7}$. Thus the experimentally determined GVDOS contains a considerable excess at the low energies.

The inset in Fig. 12 (bottom panel) compares ''Debye DOS'' calculated via Eq. (12) with the total phonon DOS for the Al_3Ni and *d*-ANC structures. However, our calculation does not reproduce the ω dependence of the amount of the localized modes: as mentioned above, the GVDOS scales approximately with ω^2, which is apparently not true in our calculation with the SE potentials. Secondly, while the acoustic signal can be clearly followed experimentally up to $E>10$ meV,[7] in our calculation *all* modes rapidly localize above $\sim$3 meV.

G. Spring model

When comparing the phonon spectrum with the experimental data, we were primarily concerned with the constraints coming from (i) the position of the main maximum of the GVDOS (corresponding to the maximum of the TM partial phonon DOS) as a fraction of the total phonon energy range, (ii) the sound velocities, and (iii) the Al and TM partial Debye-Waller factors. In order to elucidate the interplay between these factors, we designed a simple spring model, based on the nearest-neighbor interactions up to $\sim$3.2 Å, and the O-$Al_{13}Co_4$ structure model derived from the diffraction data.[21]

In the spring model, the force-constant matrix is usually modeled as a function of the distance between pairs of atoms. However, we first used an extremely simple model in which the spring constants $\phi_{\alpha\beta}$ (α and β stands for the elements Al or Co; we abbreviate $A\equiv$Al and $B\equiv$Co) do not depend on the bond length. The constant $\phi_{AA}=1.36$ eV/Å^2 was fixed at the value fitting best the fcc Al phonon spectrum, and the Al-TM coupling constant $\phi_{AB}=2.18$ eV/Å^2 to the sound velocities experimentally observed in *d*-AlNiCo.[25] The resulting phonon spectra are shown in Fig. 14 as a solid line. The Al partial DOS has a maximum near 30 meV and a shoulder near 40 meV, while the TM partial exhibits a narrow split maximum near 20 meV. The partial Debye-Waller factors are $B_{Al}=0.54$ and $B_{TM}=0.48$ Å^{-2}. Notice that the typical ratio of B_{Al}/B_{TM} is $\sim$1.4–1.6 from the diffraction data (Table IV).

In our second variant of the spring model, we let the ϕ_{AA} force constant linearly decrease within the first shell, reflecting the fact that in the complex structures, there is a distribution of the nearest-neighbor distances, with some anomalously short bonds corresponding to a large force constant and bonds longer than 2.86 Å that are expected to have a very weak spring constant according to the Al-Al pair potential. We again fixed the $\phi_{AA}=1.36$ eV/Å^2 at 2.86 Å, but adopted a slope $d\phi/dR=-5.0$ eV/Å^3 and set $\phi_{AB}=3.27$ eV/Å^2 to fit the measured sound velocity in *d*-AlNiCo. The phonon spectra of this model are shown in the same figure as a dashed line. The Debye-Waller factors are $B_{Al}=0.53$ and $B_{TM}=0.37$ Å^{-2}. Interestingly, the B_{Al} is about the same as in the previous model [the small amount of excess states at low energies cancel with much larger excess at higher energies due to the $1/\omega$ factor in the integrand of Eq. (5)].

The difference between the phonon spectra of the two models can be readily explained. The distance-dependent constant ϕ_{AA} provides extra Al states at both low and high energies. (Note that this also characterized the difference between the phonon DOS of Al_3Ni and Al_9Co_2Ni, see Sec. IV C.) Secondly, the TM partial DOS becomes broader and its maximum shifts towards higher energies, as could be expected from the stronger Al-TM coupling in the second model.

Clearly none of these simple models provides a plausible comparison with the experimental GVDOS. While further refinement of the spring model by including outer neighbor shell springs becomes a rather complicated task (the more sophisticated spring models were developed by one of us[33]), clearly it is the nearest-neighbor interaction that dominates the gross features of the GVDOS. However, the much closer fit of the experimental GVDOS by oscillating pair potentials reflects the highly nontrivial interplay between the oscillating potentials and the structure.

H. Temperature dependence of the Debye-Waller factor

The occurrence of the phonon instability that we encountered especially with the SE potentials motivated a series of molecular-dynamics cooling runs performed between the temperatures of $T=300-50$ K, as described in Sec. III B. (We do not report here on the simulations with GPT potentials because of the problematic first minimum of the Co-Co interaction.) An easily accessible quantity not particularly sensitive to the equilibration times is the Debye-Waller factor B^{MD} defined by Eq. (9). This is directly comparable to the classical high-temperature approximation [Eq. (10)] of the ''harmonic'' Debye-Waller factor [Eq. (6)], whose temperature dependence arises from the thermal occupation of the $T=0$ K phonon states. At $T=300$ K, the classically approximated Debye-Waller factor is 4–5 % smaller than the accurate quantum-mechanics result.

It should be noted that any deviations from the linear T dependence of $B(T)$ may only be due to anharmonic effects. Moreover, since we keep the volume of the unit cell fixed, these effects are also *not* quasiharmonic, which is usually a leading correction to the harmonic temperature dependence of the Debye-Waller factor.

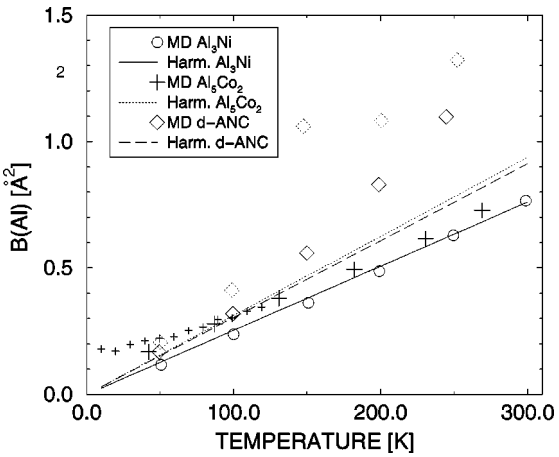

FIG. 15. Temperature dependence of the partial Al Debye-Waller factor, obtained from molecular dynamics cooling runs from $T=300$ down to 50 K (symbols) (SE potentials). The classical harmonic approximation of the phonon Debye-Waller factor is shown as lines.

In Fig. 15 we show three patterns of the $B_{Al}^{MD}(T)$ behavior for Al atoms (the TM partials turn out to behave normally in all cases): $B_{Al}^{MD}\sim B_{Al}$ for the Al_3Ni structure, $B_{Al}^{MD}<B_{Al}$ for Al_5Co_2, and $B_{Al}^{MD}>B_{Al}$ for the *d*-ANC model. While Al_3Ni shows no sign of instability from the phonon spectrum calculation and $B_{Al}^{MD}(T)$ is accurately described by the classical approximation, MD annealing together with the supercell model was necessary to avoid the phonon instability in Al_5Co_2. Interestingly, above $T=200$ K the $B_{Al}^{MD}(T)$ of Al_5Co_2 is linear and very close to that of Al_3Ni, but below $T=200$ K it exhibits an excess fluctuation of $\langle u^2\rangle$ (i.e. when $E_{kin}=E_p=\frac{3}{2}k_BT>25$ meV). We conjecture that this is due to a peculiar anharmonicity of the potential energy surface near its minimum; this has been confirmed by a longer cooling run from $T=120$ down to 10 K (smaller plus symbols in the figure). Thus we expect that the $T=300$-K B_{Al} value reported in Table III for Al_5Co_2 is overestimated.

On the other hand, $B_{Al}^{MD}(T)$ of *d*-ANC shows an excess increasing with temperature, compared to the normal harmonic behavior. This excess is due to the degeneracy of the equilibrium positions of some Al sites, in particular Al(4) [see Figs. 1(e) and 1(f)] with $B_{Al(4)}^{MD}\sim 2.6$ Å^2 at $T=300$ K. These sites form implausibly short bonds of ~ 1.8 Å in the idealized model, and the degeneracy is related to the many energetically nearly equivalent ways of breaking the decagonal symmetry of the cluster as the short bond relaxes under the action of forces. At room temperature, it is difficult to check whether the large measured B_{Al}^{MD} does not already incorporate an excess due to the onset of self-diffusion; a 10-times longer run confirmed that the B_{Al} evolves with the time (dotted diamonds in the figure). This matter is further discussed in the proceeding section.

I. High-temperature atomic configurations

We performed an additional MD annealing run at $T=1000$ K for the *d*-ANC model with the schedule described

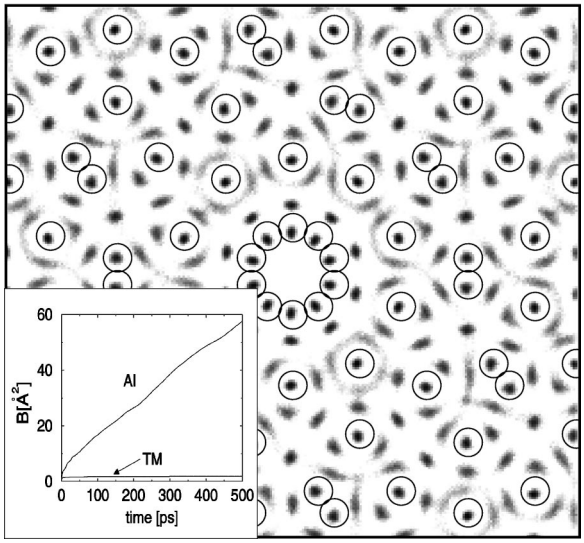

FIG. 16. Atomic density map of the *d*-ANC model from MD annealing at $T=1000$ K, projected along the pseudodecagonal axis (SE potentials, 500 samples). Large circles mark idealized positions of the Co atoms.

in Sec. III B. We recorded the time evolution of $\langle u^2 \rangle$ and projected the atomic configurations into 250×250 pixels perpendicularly to the ''periodic'' axis. Figure 16 presents clear evidence that the strongly localized low-energy states found in harmonic analysis at $T=0$ K are not a precursor of an instability: the structure is clearly stable due to the rigidity of the network of the TM atoms that can be ascribed to the strong nearest-neighbor interaction between the Al-TM pairs. Interestingly, the empty position projecting on the center of the columnar cluster, apparently capable of accommodating an atom, remains unoccupied throughout the simulation run, probably due to the strong binding with the Al(2) atoms in the surrounding 10-fold ring.

On the other hand, the typical high-temperature behavior of Al atoms is between the extrema represented by Al(2) and Al(4) atoms [see Fig. 1: Al(2) has a well-defined equilibrium position, while Al(4) shows up in the MD map as streaks]. The inset shows the time evolution of the Debye-Waller factor *B*; the slope is approximately linear, evidencing self-diffusion of Al.

V. SUMMARY AND CONCLUSIONS

We have performed an extensive analysis of the vibrational properties of the selected crystalline structures occurring in the Al-Ni-Co phase diagram, using two sets of realistic Al-Co pair potentials (and treating the Ni atom as Co): *ab initio* potentials derived from the generalized pseudopotential theory[2] (GPT), and the semi-empirical potentials[1] (SE). Our main goal was to assess the impact of the structural complexity on the character of the vibrational modes. This motivation guided our choice of the crystalline structures: Al_9Co_2Ni, O-$Al_{13}Co_4$, and the *d*-ANC approximant model are closely related to the decagonal quasicrystal, while the Al_3Ni and Al_5Co_2 phases have rather simple structure with few Wyckoff positions.

The phonon DOS of Al_3Ni and Al_5Co_2 exhibits a pronounced bandlike structure, but the features are well resolved and are at least a few meV wide, due to the predominantly extended character of the eigenmodes. In contrast, the phonon DOS of the complex structures is dominated by broad features, with a finer structure superimposed on the top. The structural complexity also gives rise to extra localized states at both ends of the phonon energy spectrum; the localized states at unusually low energies appear to be a distinct signature of the dynamics in the complex Al-Co (and presumably Al-TM) structures with the relationship to the quasicrystals. In the long-wavelength limit, the experimentally determined GVDOS of *d*-AlNiCo exhibits an excess phonon DOS, compared to the Debye DOS calculated from the experimentally measured sound velocities in *d*-AlNiCo. We tentatively attribute the excess states to the aforementioned localized excitations. However, our calculation does not reproduce the ω dependence of the density of these states.

The generalized vibrational DOS (GVDOS) of the *d*-ANC approximant model structure and O-$Al_{13}Co_4$ calculated using both sets of pair potentials explain the gross features of the experimentally determined GVDOS of the two phases: in particular, the maximum occurring between 25–30 meV is due to the partial DOS of the TM atom, while the broad Al band extends up to 60 meV.

The SE potentials applied to the variety of structures at a valence electron density close to that of the fcc Al exhibit a tendency towards marginal dynamical instability, most likely due to a shelflike feature at the typical nearest-neighbor Al-Al distance. However, the instability is marginal, mainly because of the strong Al-Co interaction: the network of Co atoms in the *d*-ANC approximant model structure remains rigidly stable in a molecular-dynamics annealing up to at least $T=1000$ K, while a fraction of Al atoms displays a diffusive motion.

The isotropic Debye-Waller factors calculated from the phonon density of states are in general smaller than those determined from the diffraction data. This trend is pronounced for GPT potentials, and presumably indicates that the Al-Co interaction derived from the GPT is too strong. Additional indication supporting this conjecture is that the TM partial DOS is shifted by a few meV to higher energies relative to the maximum of the experimentally determined GVDOS, and that the sound velocities calculated for the Al-Co crystals studied here are in general higher than the experimentally determined sound velocity in *d*-AlNiCo.

We paid special attention to the case of O-$Al_{13}Co_4$ where we expected the fractional-occupancy factors might show an appreciable impact on the vibrational properties. Rescaling uniformly the volume and varying the fractional occupancy, we find that the GPT potentials match the experimental GVDOS better at higher volumes compared to the volume for which they were evaluated. Such a treatment is of course not rigorous, and the full treatment of this problem would require application of a volume-dependent set of potentials, determination of the equilibrium volumes for each model with certain occupancy factors including the volume potential energy term, as well as the vibrational energy into the

free energy subject to minimization. Such a task remains a challenge for the future.

Interestingly, the dynamical properties of the Al_5Co_2 structure are anomalous for both sets of the pair potentials. In the SE potentials case, the phonon DOS exhibits shoulders at both ends of the spectrum, indicating the presence of extremely soft extended modes and extremely hard, partially localized modes. With the GPT potentials, the sound velocities exhibit striking, probably unrealistic, anisotropies. Thus, we suggest this structure is a candidate for detailed experimental exploration.

ACKNOWLEDGMENT

We gratefully acknowledge partial support from the DFG, Grant No. Su 176 3-2.

[1] R. Phillips, J. Zou, A. E. Carlsson, and M. Widom, Phys. Rev. B **49**, 9322 (1994).
[2] J. A. Moriarty and M. Widom, Phys. Rev. B **56**, 7905 (1997).
[3] M. Mihalkovič, W.-J. Zhu, C. L. Henley, and R. Phillips, Phys. Rev. B **53**, 9021 (1996).
[4] M. Widom and J. A. Moriarty, Phys. Rev. B **58**, 8967 (1998).
[5] M. Quilichini and T. Janssen, Rev. Mod. Phys. **69**, 277 (1997).
[6] M. Boudard, M. de Boissieu, S. Kycia, A. I. Goldman, B. Hennion, R. Bellisent, M. Quilichini, R. Currat, and C. Janot, J. Phys.: Condens. Matter **7**, 7299 (1995).
[7] F. Dugain, M. de Boissieu, K. Shibata, R. Currat, T. J. Sato, A. R. Kortan, J. B. Suck, K. Hradil, F. Frey, and A. P. Tsai, Eur. Phys. J. B **7**, 513 (1999).
[8] J. Los, T. Janssen, and F. Gähler, J. Phys. I **3**, 1431 (1993).
[9] M. Windisch, J. Hafner, M. Krajčfi, and M. Mihalkovič, Phys. Rev. B **49**, 8701 (1994).
[10] M. Krajčfi and J. Hafner, J. Non-Cryst. Solids **192&193**, 338 (1995).
[11] A. D. Bianchi, E. Felder, M. Kenzelmann, A. D. Chernikov, and H. R. Ott, in *Proceedings of the Sixth International Conference on Quasicrystals*, edited by S. Takeuchi and T. Fujiwara (World Scientific, Singapore, 1997), p. 471.
[12] N. Vernier, G. Bellessa, B. Perrin, A. Zarembowitch, and M. de Boissieu, Europhys. Lett. **22**, 187 (1993).
[13] F. Bert, G. Bellessa, A. Quivy, and Y. Calvayrac, Phys. Rev. B **61**, 32 (2000).
[14] R. Sterzel, C. Hinkel, A. Haas, A. Langsdorf, G. Bruls, and W. Assmus, Europhys. Lett. **49**, 742 (2000).
[15] M. Mihalkovič, H. Elhor, and J.-B. Suck, Mater. Sci. Eng., A **294-296**, 654 (2000).
[16] W. Steurer, T. Haibach, B. Zhang, S. Kek, and R. Lück, Acta Crystallogr., Sect. B: Struct. Sci. **49**, 661 (1993).
[17] K. Hiraga, W. Sun, and A. Yamamoto, Mater. Trans., JIM **35**, 657 (1994).
[18] M. Döblinger, R. Wittmann, D. Gerthsen, and B. Grushko, Mat. Sci. Eng., A **294-296**, 131 (2000).
[19] P. Villars and L. D. Calvert, *Pearson's Handbook of Crystallographic Data for Intermetallic Phases* (American Society for Metals, Mats. Park, OH, 1991).
[20] Y. Grin, K. Peters, U. Burkhardt, K. Gotzmann, and M. Ellner, Z. Kristallogr. **213**, 364 (1998).
[21] J. Grin, U. Burkhardt, M. Ellner, and K. Peters, J. Alloys Compd. **206**, 243 (1994).
[22] E. Cockayne and M. Widom, Philos. Mag. A **77**, 593 (1998).
[23] E. Cockayne and M. Widom, Phys. Rev. Lett. **81**, 598 (1998).
[24] K. Yamamoto, M. Jono, and Y. Matsuo, J. Phys.: Condens. Matter **11**, 1015 (1999).
[25] M. A. Chernikov, H. R. Ott, A. Bianchi, A. Migliori, and T. W. Darling, Phys. Rev. Lett. **80**, 321 (1998).
[26] P. J. Steinhardt, H.-C. Jeong, K. Saitoh, M. Tanaka, E. Abe, and A. P. Tsai, Nature (London) **396**, 55 (1998).
[27] R. J. Bell and D. C. Hibbins-Butler, J. Phys. C **8**, 787 (1975).
[28] R. A. Brand, J. Voss, A.-J. Dianoux, and Y. Calvayrac, Phys. Rev. B **62**, 8849 (2000).
[29] M. Mihalkovič, F. Dugain, and J.-B. Suck, J. Non-Cryst. Solids **205-207**, 701 (1996).
[30] F. Dugain, *Generalized Vibrational Density of States of* $Al_{13}Co_4$ (unpublished).
[31] J. Hafner and M. Krajčfi, J. Phys.: Condens. Matter **5**, 2489 (1993).
[32] C. L. Henley and V. Elser, Philos. Mag. B **53**, L59 (1986).
[33] H. Elhor (unpublished).
[34] J. Grin, U. Burkhardt, and M. Ellner, Z. Kristallogr. **209**, 479 (1994).
[35] K. Gotzmann, Ph.D. thesis, Universität Stuttgart, 1998.
[36] D. L. McDonald, Acta Crystallogr. **23**, 185 (1966).